RSC Advances

ROYAL SOCIETY OF CHEMISTRY

www.rsc.org/advances

Journal Name

RSCPublishing

ARTICLE

Room temperature crystallization of highly luminescent lanthanide-doped CaF_2 in nanosized droplets: first example of synthesis of metal halogenide in miniemulsion with effective doping and size control

Cite this: DOI: 10.1039/x0xx00000x

Received 00th January 2012,
Accepted 00th January 2012

DOI: 10.1039/x0xx00000x

www.rsc.org/

Paolo Dolcet,[a,b] Antonin Mambrini,[a,c] Marco Pedroni,[d] Adolfo Speghini,[d] Stefano Gialanella,[e] Maurizio Casarin,[a] Silvia Gross[a,b,*]

In this paper, we report the first successful preparation of calcium fluoride by miniemulsion. Calcium fluoride is a widely investigated material known to be an excellent host for luminescent lanthanide ions; herein we report an easy and reproducible way to achieve the controlled doping of CaF_2 nanostructures (Ca:Ln = 50:1, with Ln = Sm^{III}, Gd^{III} and Tb^{III}) at room temperature, through the miniemulsion approach. The materials are thoroughly characterized from a structural, morphological and functional point of view, by the combined use of several techniques, i.e. X-ray Diffraction (XRD), X-Ray Photoelectron Spectroscopy (XPS), Inductively Coupled Plasma Mass Spectrometry (ICP-MS), Scanning and Transmission Electron Microscopy (SEM and TEM respectively) and photoluminescence (PL) Spectroscopy. In addition, to get further insight into the local structure around the dopants, Extended X-ray Absorption Fine Structure (EXAFS) experiments is performed.

Introduction

Similarly to their oxide- and sulfur-based counterparts, rare earth-doped metal fluoride compounds are very attractive materials for a wide variety of potential applications, including photonics, light amplification, anti-fraud labeling, and optical bioimaging. Moreover, they also found application as advanced phosphors and in display monitors[1]. On the other hand, metal fluorides present additional advantages, in particular a high transparency in a wider wavelength window, ranging from infrared to vacuum ultraviolet (VUV), low defectivity, and a low phonon energy, resulting in a decreased non-radiative transition probability of the embedded luminescent ions and enhanced luminescent properties. In addition, these ions may show near infrared (NIR)–to-red or NIR–to-NIR upconversion properties, of particular importance for biomedical purposes. In fact, an excitation in the NIR region (around 1000 nm) coupled with emission also in the NIR (or in the red) is very advantageous, due to the high transparency of the biological fluids in this region, together with a low tissues damage and an almost total absence of autofluorescence[2].

Among the fluoride compounds, CaF_2 is particularly appealing as a consequence of its stability and non-hygroscopic behavior; moreover, thanks to its crystal structure (consisting of a simple cubic array of fluoride ions with every alternate cube occupied by the divalent cation Ca^{II}), it is a good host for doping ions, also in high concentrations[3]. Due to the similarity in ionic radii, trivalent lanthanide ions can indeed easily substitute the calcium cation, even if charge compensation (typically through the presence of interstitial fluoride ions) is required[2]. In particular, it was demonstrated that lanthanide ions in low concentration (0.1 % with respect to the Ca^{II} ion) can enter in centers with C_{4v}, C_{3v} and also O_h symmetry[4–6].

In addition, calcium fluoride shows an excellent biocompatibility[7], and doped CaF_2 nanostructures are then appealing as bioimaging contrast agents[8–11].

Ln-doped CaF_2 nanostructures have been prepared by a wide variety of methods such as sol-gel[12], solvo/hydrothermal methods[2,13,14], polyol-mediated[15], thermal decomposition of

precursors [16], and colloidal techniques, such as microemulsion [1,17].

Conversely, to the best of our knowledge, no report on the use of miniemulsions for the room temperature preparation of such crystalline systems is reported yet in the literature. On contrary to microemulsions, miniemulsions are kinetically stabilized systems rather than thermodynamically stable ones, and, throughout the reaction, the droplets constituting such systems maintain their identity throughout the reaction, thus being perfectly suited to spatially confine the crystallization of the desired materials [18]. Whereas most of the methods present in the literature cited above (with the exception of microemulsions) require a high temperature step (T > 100°C), the miniemulsion approach permits to obtain crystalline materials already at room temperature, allowing simultaneously a good control on the particles size and morphology. Furthermore, with respect to microemulsions, miniemulsions usually require a much smaller amount of surfactant to reach colloidal stability, thus being more cost-effective and easier to purify. In recent times, we successfully exploited the miniemulsion approach for the controlled synthesis of doped ZnO, ZnS and $M(OH)_2$ (M=Ca, Mg) nanostructures [19–22].

In this work, we report the synthesis of rare earth-doped calcium fluoride nanoparticles (Ln=Sm^{III}, Gd^{III} and Tb^{III}, with Ca:Ln=50:1 molar ratios), prepared by a miniemulsion approach based on the mixing of two miniemulsion, containing the Ca^{2+}/dopant and F^- sources respectively, and inducing the co-precipitation in the confined space of the droplets.

Results and discussion

The nanostructures were prepared using NaF as a simple fluoride source, much less hazardous and toxic than HF. The miniemulsions produced by mixing and ultrasonication of the two starting emulsions were firstly analyzed by dynamic light scattering (DLS), in order to investigate the average size of the droplets obtained by this method. Such analyses (data not shown), performed for pure CaF_2 samples, revealed a mean hydrodynamic radius of 180 nm, showing also a good reproducibility of the method proposed. After aging overnight, the nanostructures formed a fine precipitate and the corresponding powders were separated by centrifugation. These powders were firstly characterized by X-ray diffraction, to assess the actual formation of crystalline materials. All samples showed the formation of fluorite (JCSD PDF N: 77-2093), contemporarily evidencing the absence of spurious amorphous phases and, in the case of the doped materials, of secondary phases due to the doping ions (see Figure1). In addition, in the doped samples, a faint reflection appears at roughly 32.8°. This feature corresponds to the (200) Bragg peak, which is an allowed X-ray diffraction reflection for the fluorite structure but is usually present with negligible intensity. The increase in the intensity of this reflection arises from the difference of atomic number Z between the RE dopants and calcium and is symptomatic of successful incorporation of the RE ions in the host fluoride matrix[1,23].

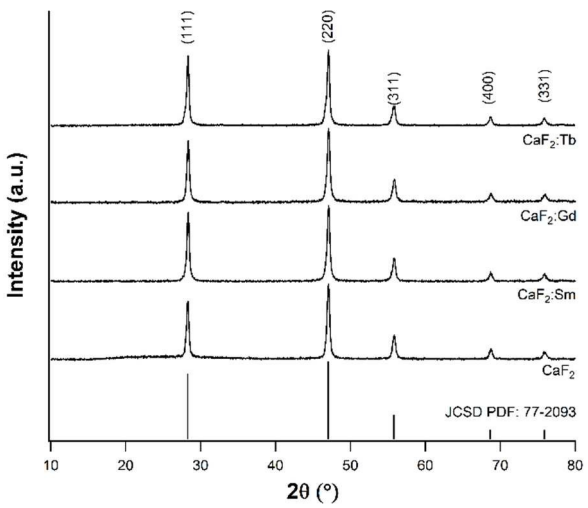

Figure 1. XRD diffractograms for pure and doped CaF_2 nanostructures

In Table 1 the crystallite sizes, determined by using the Rietveld refinement method [24,25], are reported, showing an average value of 36-37 nm. Upon insertion in the lattice, doping ions induce slight distortions and correspondingly XRD reflections shift to higher Bragg's angles; the difference is more evident in the Tb doped sample. This is not surprising, since terbium has the smallest ionic radius of the three dopants [26,27].

Table 1. Average crystallite size, as determined by Rietveld method, lattice constants and cations ionic radii for an 8-fold coordination

Sample	Crystallite size (nm)	Ionic radius (pm)
CaF_2	36.9±0.5	Ca^{II}: 1.12
CaF_2:Sm	35.6±0.4	Sm^{III}: 1.079
CaF_2:Gd	37.0±0.4	Gd^{III}: 1.053
CaF_2:Tb	37.3±0.1	Tb^{III}: 1.04

The ultrasonication process, by producing high shear forces, induces many fission and fusion events between droplets, affecting the average droplet size and possibly the final material characteristics. In order to investigate how the final dimensions of the crystallites are influenced by this homogenization process, the ultrasonication time was varied (t=40, 60, 120 and 180 s), both for the preparation of the starting miniemulsions and the homogenization of the final one. The obtained powders were examined by XRD, and the average crystallite sizes, as determined by Rietveld refinement, are shown in Table 2.

Table 2. Influence of sonication time on crystallite sizes

Sonication time	Average crystallite size (nm)
40 s	77.8±1.3

60 s	63.1±0.5
120 s	39.9±0.5
180 s	36.9±0.5

Fascinatingly, the crystallite size showed a decrease with increasing sonication time (increasing the sonication time from 40 s to 180 s yielded a decrease in the crystallite diameter down to less than half the initial value, see Table 2). This is a very important result, confirming the key role played by ultrasounds in forming and stabilizing the nanodroplets, which therefore act as nanoreactors.

Information about nanoparticles microstructure and morphology was obtained by means of TEM and SEM microscopy. TEM micrographs (see Figure 2) prove a similar morphology characterized by the presence of grains whose size ranges between 60-100 nm, showing at the same time darker domains. Selected area diffractograms of grains show bright spots corresponding to the fluorite structure, in agreement with XRD results, contemporarily revealing the presence of a minor second phase, displayed as a faint continuous, homogeneous rings, which was identified as CaO (JCSD PDF N: 77-2010).

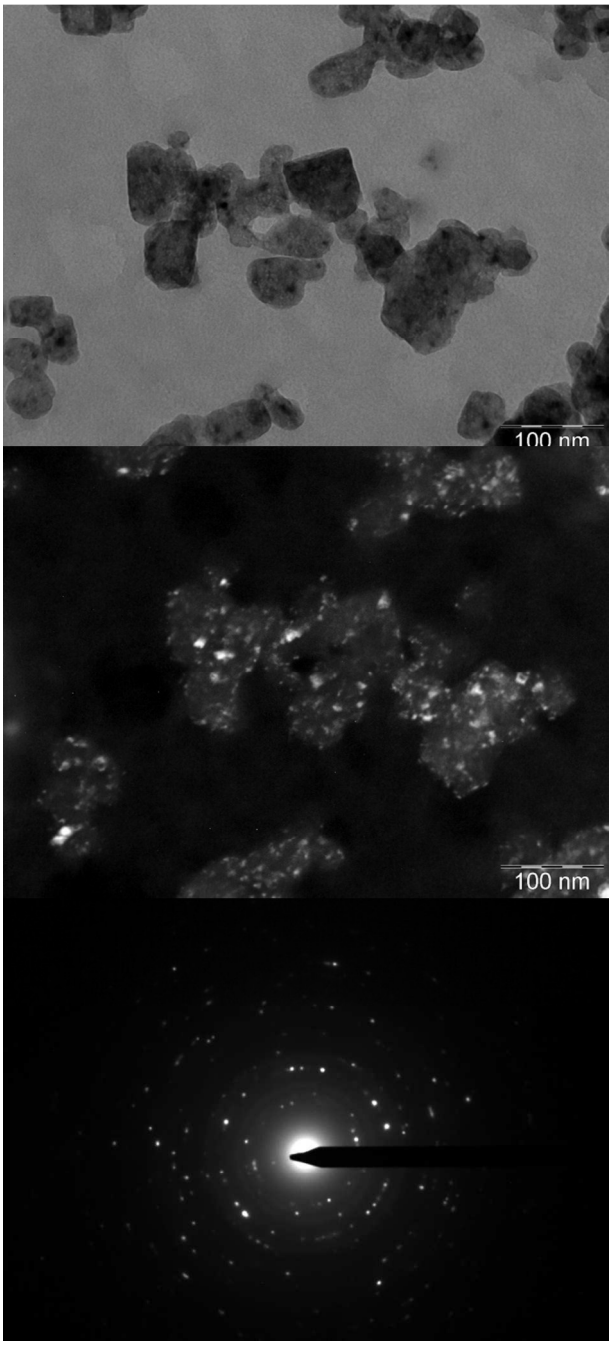

Figure 2. Bright (top) and dark (center) field TEM micrographs. Dark field images were recorded using a portion of the continuous rings found in the SAED diffractogram (bottom)

Dark field images registered by using a portion of the oxide diffraction rings evidenced that the darker domains seen in bright field are indeed oxide portions, highlighting therefore the presence of an oxide layer on the fluorite grains. SEM micrographs (see Figure 3) were consistent with TEM findings, and showed agglomerates of quasi-spherical nanoparticles whose average size is 50-100 nm. This size, comparable with the average crystallite size of around 40 nm, could mean that the particles are indeed single crystallites.

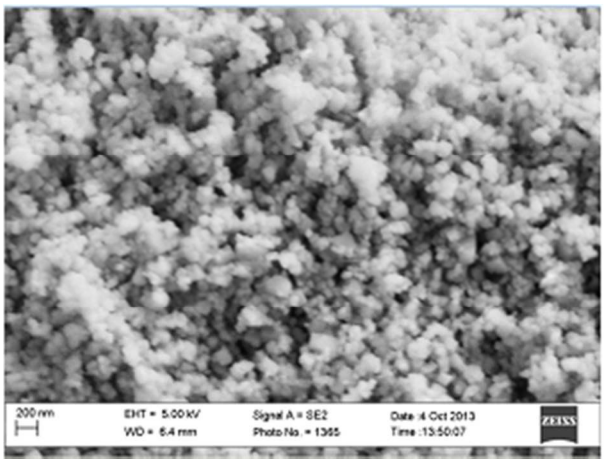

Figure 3. SEM micrograph of pure CaF_2 nanoparticles

A further confirmation of the presence of an oxide surface layer was given by XPS analysis, performed on pure and doped CaF_2 samples, the results of which are summarized in Table 3. The $Ca2p_{3/2}$ peaks present two components, one centered at 346.9-347.4 eV, compatible with the oxide ($Ca2p_{3/2}$=346.7-347.3 eV [28]), and the latter (see percentages reported in Table 3), lying at 347.5-348.2, corresponding to the fluoride (Ca2p3/2=347.8-348.1 eV [28]). F1s signals are found at 684.3-684.5 eV, values typical of calcium fluoride (F1s=684.6 eV [29]). Analogously to the $Ca2p_{1/2}$, the O1s peak can be deconvoluted into two contributions, the former centered at about 530-531 eV, compatible with CaO, and the latter, lying at higher binding energy (532-532.5 eV),

vealdue to the ethylene glycol chains in the surfactants. As for the dopant signals, the binding energy values for Sm and Gd $3d_{5/2}$ peaks are compatible with a Ln^{III} ion in a fluoridic environment, while, for the Tb doped sample, the signal-to-noise ratio is too low to discriminate accurately the $3d_{5/2}$ signal. Interestingly, the Gd doped sample is also the one for which the CaO components of the $Ca2p_{3/2}$ peak is more relevant.

Table 3. Binding energy values determined by XPS

Sample	$Ca2p_{3/2}$ (eV)	F1s (eV)	Dopant $3d_{5/2}$ (eV)	O1s (eV)
CaF_2	347.4 (34 %) 348.1 (66 %)	684.5	-	531.0 532.4
CaF_2:Sm 50:1	346.9 (16 %) 347.6 (84 %)	684.3	1083.5	531.5 532.5
CaF_2:Gd 50:1	346.7 (25 %) 347.5 (75 %)	684.4	1187.0	530.6 532.2
CaF_2:Tb 50:1	347.4 (48 %) 348.2 (52 %)	684.5	Not available	530.0 532.1

From the XPS spectra of selected regions, the amount of each detected element was determined. As it can be seen from Table 4, all samples present high amounts of carbon, due to the presence of surfactants adsorbed on the surface and external contamination. The Ca:F atomic ratio was determined to be, within the experimental error, in accordance to the nominal 1:2 ratio. The best agreement was found for the Sm doped sample, which presented a lower carbon content. At variance to that, this content was higher for the Gd sample, thus partially explaining the higher CaO content and low signal-to-noise ratio for Gd, since, due to surface specificity of XPS, the analysis is strongly affected by contamination.

Table 4. Atomic percentages for CaF_2 nanostructures, as determined by XPS

Sample	C %	O %	Ca %	F %	F:Ca	Dopant %
CaF_2	65.0	12.3	8.4	14.3	1.7	-
CaF_2:Sm	58.6	11.5	10.0	19.6	2.0	0.3
CaF_2:Gd	66.2	11.1	7.9	14.6	1.9	0.1
CaF_2:Tb	65.6	11.2	7.3	15.9	2.2	Not available

The successful embedding of dopants was confirmed also by ICP-MS, revealing an excellent agreement between nominal and experimental atomic ratios, as reported in Table 5.

Table 5. ICP-MS results for doped CaF_2 nanostructures (Confidence interval: 95 %)

Sample	Nominal ratio	Experimental ratio
CaF_2:Sm	50:1	51 ± 4
CaF_2:Gd	50:1	49 ± 4
CaF_2:Tb	50:1	55 ± 6

To assess perturbations induced in the crystal lattices upon doping, the obtained powders were also investigated by Raman spectroscopy (λ_{exc}=532 nm) Spectra are characterized by an intense signal at around 320-322 cm^{-1} (see Figure 4), a distinctive phonon vibrational band of cubic CaF_2, corresponding to the T_{2g} vibrational mode and due to fluorine ions oscillating towards each other[30]. For pure CaF_2 this signal is found at 320 cm^{-1}, for CaF_2:Sm and CaF_2:Gd at 321 cm^{-1}, while for CaF_2:Tb this peak is at 322 cm^{-1}. The peaks for the Gd doped sample and pure CaF_2 almost coincides, meaning that the dopant ions do not induce relevant lattice distortions. This possibly indicates an efficient dilution of the Ln ion in the host matrix or, on the other hand, hints to possible segregation effects. For the Sm doped sample, the peak position is close to that of the pure CaF_2, but the band shows a broadening, symptomatic of slight lattice distortions. Consistently with what determined by XRD, the greatest distortions were reed for the Tb doped sample.

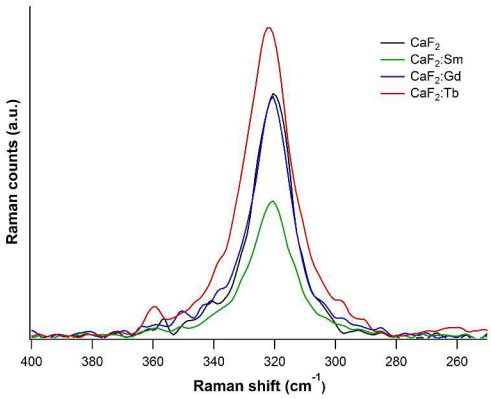

Figure 4. Raman spectra for pure and doped CaF_2 nanoparticles

To shed light on the actual local environment of the dopant, its valence and coordination geometry in the matrix, influencing the PL behavior, X-ray Absorption (XAS) experiments (XANES and EXAFS) were performed at the dopants L_3-edges. In Figure 5a, XANES spectrum of Tb L_3-edges is exemplarily reported.

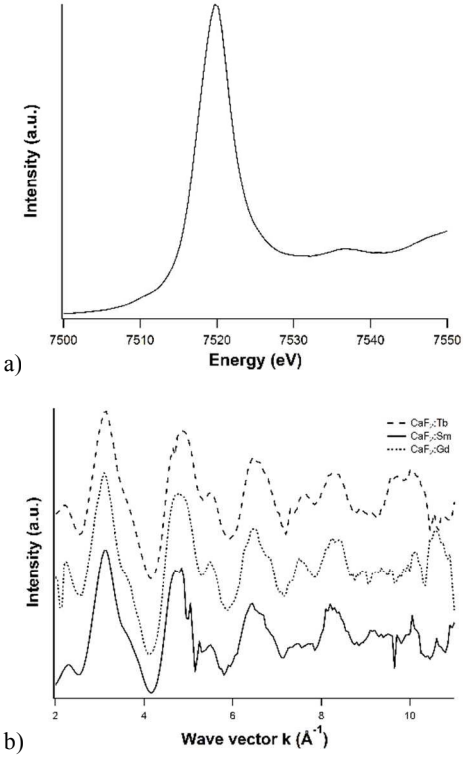

Figure 5. Dopant L_3-edge a) XANES spectrum of Tb-doped CaF_2 nanoparticles, and b) dopants EXAFS functions

Sm, Gd and Tb XANES spectra are dominated by intense white lines, since the transition involved is the $2p_{3/2} \rightarrow 5d$, towards empty d orbitals. Furthermore, the 2p core holes lifetime broadening is relevant (3.5-4.5 eV), and therefore much of the near-edge structure is lost. On the other hand, the three edges are asymmetrical, symptomatic of the presence of two underlying components describing the crystal field splitting of the 5d orbitals, with the t_{2g} levels energetically lower than the e_g levels, assuming, for simplicity, local cubic (O_h) symmetry[31].

Table 6. Numeric results from fitting the experimental EXAFS spectra with theoretical models

Sample	Coordination number	Ln-F Distance (Å)	Debye-Waller factor σ^2 (Å^2)
CaF_2:Sm	7.7 ± 0.8	2.33 ± 0.02	0.0065 ± 0.0020
CaF_2:Gd	7.8 ± 1.1	2.32± 0.03	0.0070 ± 0.0028
CaF_2:Tb	8.2 ± 0.7	2.29 ± 0.02	0.0091 ± 0.0017

As far as the EXAFS region is concerned, the corresponding functions are reported in Figure 5b, and the behavior of the different samples is similar, evidencing therefore analogous chemical environment. First shell fitting (Table 6) revealed that the lanthanide ions are indeed found in a fluoridic environment, with coordination number compatible, within the experimental error, with the picture of substitutional doping, since in the fluorite structure Ca ions are surrounded by 8 fluoride anions [32]. For the Gd-doped sample, the lower quality of the data registered is reflected in higher uncertainties.

As already mentioned, these materials are interesting for their optical properties, as calcium fluoride is a good host for lanthanide ions. The photoluminescence (PL) spectrum of CaF_2:Tb sample (Figure 6a, solid line), upon excitation at 355 nm, is characterized by the typical Tb^{III} emission bands [33,34], involving transitions from the $^5D_4$ excited level to the ^7F_J levels (J = 3, 4, 5 and 6), as labeled in Figure 6a. The spectrum is dominated by the $^5D_4 \rightarrow {}^7F_5$ transition. The emission decay curve (shown in Figure 6b) does not present an exponential behavior, with an effective decay time of 8.3±0.3 ms, a value higher than those usually reported in the literature for such an ion, embedded in CaF_2 nanocrystals, for example prepared by thermal decomposition of the corresponding trifluoroacetates (6 ms[16]) or as xerogels (3 ms[35]). This increase in the decay time is a further evidence of the successful lanthanide doping in the CaF_2 crystalline structure.

Journal Name RSCPublishing

ARTICLE

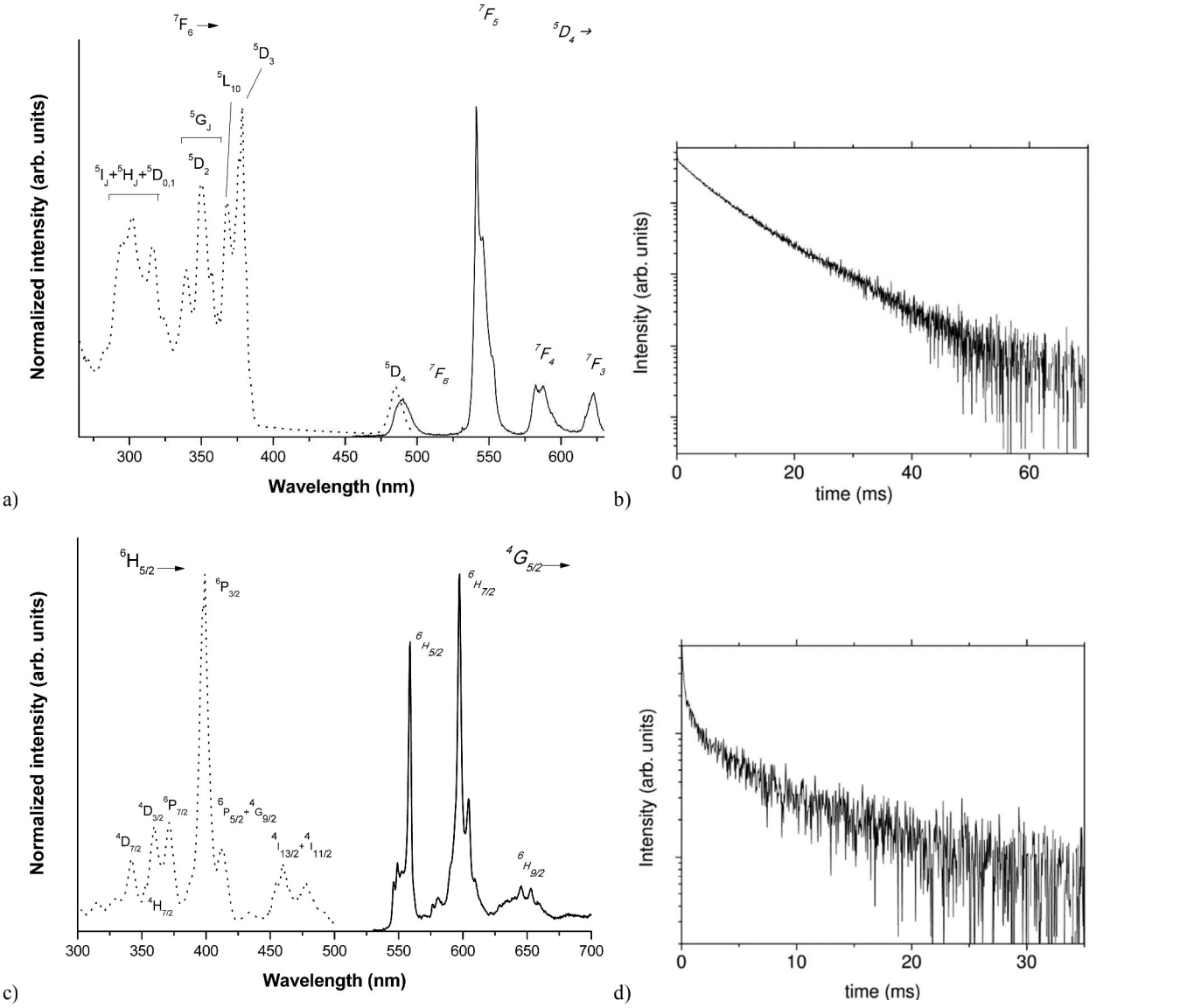

Figure 6. Normalized excitation (dotted lines, λ_{emi} = 604 nm) and emission spectra (solid lines, λ_{exc} = 355 nm) of a) CaF_2:Tb and c) CaF_2:Sm, and corresponding RT emission decay curves (b and d respectively)

The PL spectrum (shown in Figure 6c) of the CaF_2:Sm sample presents emission bands involving transitions from the excited $^4G_{5/2}$ level to the lower energy ^6H_J levels (J = 5/2, 7/2 and 9/2). The weak but observable band around 650 nm is due to the electric dipole (ED) allowed $^4G_{5/2}$→$^6H_{9/2}$ transition of the Sm^{3+} ions. This band has no magnetic dipole (MD) character[36,37] and therefore it is due to lanthanide ions accommodated in sites without inversion symmetry. On the other hand, the quite strong band around at 550 nm due to the $^4G_{5/2}$→$^6H_{5/2}$ transition has a strong MD contribution (MD allowed, $\Delta J=0$[36,37]), while the strongest band around 600 nm is due to the $^4G_{5/2}$→$^6H_{7/2}$ transition and it has both ED and MD contributions (MD allowed, $\Delta J=1$[36,37]). It is worth to underline that Sm^{3+} ions in sites with inversion symmetry (e.g. cubic sites) show bands due to both $^4G_{5/2}$→$^6H_{5/2}$ and $^4G_{5/2}$→$^6H_{7/2}$ transitions but not to the $^4G_{5/2}$→$^6H_{9/2}$ one, as found for Sm^{3+} doped CeO_2 thin films[38].

The present spectroscopic behavior is therefore compatible with lanthanide ions accommodated in more sites with different local symmetries[6,39], entailing also the presence of a cubic symmetry, as evidenced by EXAFS measurements. As observed for the Tb doped CaF_2 sample, the emission decay curve (Figure 6d) has a pronounced non-exponential behavior and the effective decay time is 11±1 ms. This value is notably higher than the value found in literature (6 ms)[40], suggesting a higher average symmetry around the lanthanide ions.

The corresponding excitation spectra (see Figure 6a and 6c, dotted lines) present bands originating from *4f-4f* transitions of the lanthanide ions. The excitation spectrum for the Tb^{3+} doped sample is very similar to that obtained for a Tb^{3+} doped CaF_2 sample prepared by a coprecipitation route using water as a solvent[8]. Similarly, the Sm^{3+} excitation spectrum is in agreement with that reported for Sm^{3+} doped CaF_2 nanocrystals in transparent glass ceramics, investigated by Lakshminarayana et al. [41].

Experimental section

Materials

In a typical synthesis, two identical mixtures, A and B, were prepared by dispersing 100 mg of Igepal® CO-630 (0.16 mmol) and 300 mg of Brij® 52 (0.9 mmol) in 8.0 g of cyclohexane. Subsequently, 2 ml of an aqueous 0.5 M $Ca(NO_3)_2$•$4H_2O$ precursor solution (1.0 mmol) were added to mixture A and stirred, yielding emulsion A', while 2 ml of aqueous solution of 1 M NaF (2.0 mmol) were added to mixture B, to generate, after mechanical stirring, emulsion B'. In the case of the doped systems, 0.04 mmol of a dopant metal salt (either $Sm(CH_3COO)_3$•xH_2O, $Gd(NO_3)_3$•$6H_2O$ or $Tb(NO_3)_3$•$5H_2O$) were added to the Ca containing solution, to achieve a final Ca:M molar ratio of 50:1. Both emulsions were then separately sonicated for 3 minutes. The resulting miniemulsions A' and B' were mixed together and sonicated again, with unchanged time and amplitude. The suspension was allowed to stand for one night. The precipitate that formed was separated by centrifugation (10 krpm for 10 minutes) and washed with deionized water. The procedure of centrifugation and washing was repeated five times.

XPS analysis

Powder samples were investigated by XPS with a Perkin-Elmer ϕ 5600ci instrument using standard Al-K_α radiation (1486.6 eV) operating at 350 W. The working pressure was < 5×10^{-8} Pa. The calibration was based on the binding energy (BE) of the Au $4f_{7/2}$ line at 83.9 eV with respect to the Fermi level. The standard deviation for the BE values was 0.15 eV. Reported BEs were corrected for charging effects, assigning the BE value of 284.6 eV to the C1s line of carbon[42]. Survey scans were obtained in the 0 - 1350 eV range (pass energy 187.5 eV, 1.0 eV $step^{-1}$, 25 ms $step^{-1}$). Detailed scans (29.35 eV pass energy, 0.1 eV $step^{-1}$, 50-150 ms $step^{-1}$) were recorded for the O1s, C1s, Ca2p, F1s and dopants 3d and Auger regions. The atomic composition, after a Shirley-type background subtraction[43] was evaluated using sensitivity factors supplied by Perkin-Elmer[29]. Charge effects were partially compensated by using a charge neutraliser (flood gun). Peak assignment was carried out according to literature data.

X-Ray diffraction

The XRD data were collected with a Bruker D8 Advance Diffractometer equipped with a Göbel mirror by using the Cu-K_α radiation. The angular accuracy was 0.001° and the angular resolution was better than 0.01°. All experimental data were analyzed using the Material Analysis Using Diffraction (MAUD) software package[25], an original software used to work out quantitative crystallographic and microstructural information[24] using a Rietveld code.

SEM analysis

Measurements were performed by using a Field Emission (FE-SEM) Zeiss SUPRA 40VP, with a primary beam acceleration voltage of 5 kV and a conventional secondary electron detector.

TEM analysis

TEM analysis was carried out using a Philips CM12 microscope operating at 120 keV and equipped with an EDXS, which allows localized chemical analyses. For each sample, both images and Selected Area Electron Diffraction (SAED) patterns were collected to investigate morphology and dimensions of CaF_2 nanostructures, their crystalline nature and local chemical composition.

Micro-Raman spectroscopy

Micro-Raman experiments were performed with a with a Thermo Scientific DXR Raman microscope, operating in the range 100-6000 cm^{-1}, with a λ = 780 nm solid state laser and a 10x objective.

Luminescence spectroscopy

Luminescence measurements were performed using a tunable dye laser pumped by a Nd:YAG laser as the excitation source. The emission signal was analyzed by a half-meter monochromator (HR460, Jobin Yvon) equipped with a 150 lines/mm grating and detected with a CCD detector (Spectrum One, Jobin Yvon). The spectral resolution of the emission spectra was about 0.4 nm. The emission decay curves were measured upon pulsed laser excitation and detected with a GaAs photomultiplier (Hamamatsu) and a 500 MHz digital oscilloscope (WaveRunner, LeCroy). Excitation spectra in the UV-visible range were measured with a modular spectrofluorimeter (Horiba-Jobin Yvon, Fluorolog-3-2iHR320) with a spectral resolution of 1 nm. It is to be noted that it is possible to excite the Sm^{3+} ions with a radiation at 355 nm since at this wavelength the absorption of the Sm^{3+} ions, although not very high, is observable, as it can be seen in Figure 6c. In this region, in fact, we are exciting in the Stark levels of the $^4H_{7/2}$ level of the Sm^{3+} ions[44,45].

X-ray absorption spectroscopy

Sample preparation Samples were finely ground into a homogeneous powder with cellulose as dispersant and pressed into pellets.

Metals L_3-edges Dopant L_3-edges spectra were recorded at the 2.9 T bending magnet SuperXAS beamline at Swiss Light Source (SLS), under standard ring conditions (2.4 GeV, 400 mA). For energy selection, a Si(111) double-crystal monochromator was used. Spectra were collected in the fully

tuned configuration of the monochromator. Data were collected in transmission mode by using an ionization chamber placed downstream of the sample or, for dopants edges, in fluorescence mode, using a 13-element Ge solid state detector. Internal energy calibration was accomplished by simultaneous measurement of the absorption of an appropriate metallic foil placed between two ionization chambers situated after the sample.

Data reduction and analysis Data reduction and analysis was performed using the Demeter package[46]; in particular, background removal was performed by the Autobk routine of the Athena software, which was also used for data alignment and calibration. The extracted EXAFS function were fitted exploiting the software Artemis.

ICP-MS analysis

Chemicals and materials All reagents were of analytical grade and were used as purchased: HNO_3 (CAS Number 7697-37-2) 70%, ≥99.999% (Sigma Aldrich), $HClO_4$ 70% RP Normapur (Prolabo, France). Zn (100mg/l) was present in the multi-element standard Solution CPAchem Calibration Standard (MS19EB.10.2N.L1). Gd, Sm and Tb (all 1 mg/l) were present in the ICP-MS Calibration Standard (MS98B2.1.2N.L1). All solutions were prepared in MilliQ ultrapure water obtained with a Millipore Plus System (Milan, Italy, resistivity 18.2 MΩ cm−1). The ICP-MS was tuned daily using a 1 µg/l tuning solution containing ^{140}Ce, ^{7}Li, ^{205}Tl and ^{89}Y (Agilent Technologies, UK). A 100 µg/l solution of ^{45}Sc and ^{115}In (Aristar®, BDH, UK) prepared in 2% (v/v) nitric acid was used as an internal standard through addition to the sample solution via a T-junction.

Solution setup Multielement standard solutions were prepared in 2% v/v HNO_3. The calibration solutions were prepared by gravimetric serial dilution from multi-element standard solutions, at six different concentrations (min. 10 ppb–max. 1000 ppb). Calibration plots were obtained with an internal standard. All regressions were linear with a determination coefficient larger than 0.9999. To check for instrumental drift, one of the multi-element standards was analysed every 10 samples. Blank samples of ultrapure water and reagents were also prepared using the same procedures as for the samples. All blank levels obtained were subtracted appropriately.

Nanoparticles (NPs) digestion NPs doped samples (50 mg) were placed in a 25 ml digestion vials and added with 3 ml of 70% HNO_3 and 3 ml 60% $HClO_4$. Vials were heated on a hot plate at 200 ± 10 °C for 150 min. A PTFE cap was used to minimize sample loss from the vial. Vials were then cooled and the obtained solutions were diluted with 2% v/v HNO_3. All the elements were measured by using inductively coupled plasma coupled to mass spectrometer Agilent Technologies 7700x ICP-MS system (Agilent Technologies International Japan, Ltd., Tokyo, Japan,), equipped with an octupole collision cell. The instruments were optimized daily to achieve optimum sensitivity and stability according to manufacturer recommendations. All parameters were checked daily by using an in-house optimization program.

Conclusions

Lanthanide doped CaF_2 crystalline nanostructures were synthesized at room temperature by co-precipitation in the confined space of miniemulsion droplets. This approach yielded nanostructures with an average crystallite size of 37 nm. SEM and TEM micrographs evidenced the formation of aggregates of nanoparticles with sizes of about 50-100 nm. SAED also revealed the presence of a secondary phase consisting in an oxide surface layer, as also confirmed by X-ray photoelectron spectroscopy. Micro-Raman data suggested lattice distortion induced by lanthanide ions, and EXAFS outcomes indeed confirmed that these ions are surrounded by about 8 fluoride ions, compatible with a substitutional doping. From a functional point of view, the Tb and Sm doped CaF_2 samples showed luminescence, with emission typical of the lanthanide ions. Interestingly, the sonication time was found to be a key aspect in determining the crystallite size, since increasing the time leads to a decrease in the crystallite size.

Acknowledgements

Prof. Paolo Pastore and Dr. Denis Badocco (University of Padova, Italy) are kindly acknowledged for ICP analyses. A.S and M.P gratefully acknowledge the company "Performance in Lighting" (Colognola ai Colli, Verona, Italy), for financial support in the framework of the Joint Projects 2011 of the University of Verona, Italy. S.G. thanks Ministero degli Affari Esteri (MAE, Rome, Italy) and Consiglio Nazionale delle Ricerche (CNR, Rome, Italy) for financial support. P.D. thanks the University of Padova for a post-doc scholarship. Dr. Emiliano Fonda, Soleil Synchrotron Facility, is kindly acknowledged for the support during XAFS measurements, as well as Calipso Program of the European Union (EU) for financial support.

Notes and references

[a] Dipartimento di Scienze Chimiche, Università degli Studi di Padova, via Marzolo, 1, 35131, Padova, Italy.
[b] Istituto per l'Energetica e le Interfasi, IENI-CNR and INSTM, UdR, via Marzolo, 1, 35131, Padova, Italy.
[c] Universitè Paris-Sud, Le Guichet, Orsay-Ville, ou Bures-sur-Yvette.
[d] Dipartimento di Biotecnologie, Università di Verona and INSTM, UdR Verona, Strada le Grazie 15, 37134, Verona, Italy.
[e] Dipartimento di Ingegneria Industriale, Università degli Studi di Trento, Italy.
* corresponding author. E-mail: silvia.gross@unipd.it

Electronic Supplementary Information (ESI) available: [details of any supplementary information available should be included here]. See DOI: 10.1039/b000000x/

1. A. Bensalah, M. Mortier, G. Patriarche, P. Gredin, and D. Vivien, *J. Solid State Chem.*, 2006, **179**, 2636–2644.
2. M. Pedroni, F. Piccinelli, T. Passuello, M. Giarola, G. Mariotto, S. Polizzi, M. Bettinelli, and A. Speghini, *Nanoscale*, 2011, **3**, 1456–60.
3. G. Zhi, J. Song, B. Mei, and W. Zhou, *J. Alloys Compd.*, 2011, **509**, 9133–9137.
4. N. Strickland and G. Jones, *Phys. Rev. B*, 1997, **56**, 10916–10929.
5. J.-P. Wells and R. Reeves, *Phys. Rev. B*, 2000, **61**, 13593–13608.
6. J.-P. Wells and R. Reeves, *Phys. Rev. B*, 2001, **64**, 035102.

7. W. Zheng, S. Zhou, Z. Chen, P. Hu, Y. Liu, D. Tu, H. Zhu, R. Li, M. Huang, and X. Chen, *Angew. Chem. Int. Ed. Engl.*, 2013, **52**, 6671–6.

8. S. Sasidharan, A. Jayasree, S. Fazal, M. Koyakutty, S. V. Nair, and D. Menon, *Biomater. Sci.*, 2013, **1**, 294.

9. L. Zhao, A. Kutikov, J. Shen, C. Duan, J. Song, and G. Han, *Theranostics*, 2013, **3**, 249–57.

10. G. Chen, J. Shen, T. Y. Ohulchanskyy, N. J. Patel, A. Kutikov, Z. Li, J. Song, R. K. Pandey, H. Agren, P. N. Prasad, and G. Han, *ACS Nano*, 2012, **6**, 8280–7.

11. W. Yin, G. Tian, W. Ren, L. Yan, S. Jin, Z. Gu, L. Zhou, J. Li, and Y. Zhao, *Dalton Trans.*, 2014, **43**, 3861–70.

12. B.-C. Hong and K. Kawano, *Opt. Mater. (Amst).*, 2008, **30**, 952–956.

13. X. Sun and Y. Li, *Chem. Commun.*, 2003, **9**, 1768.

14. C. Pandurangappa, B. N. Lakshminarasappa, and B. M. Nagabhushana, *J. Alloys Compd.*, 2010, **489**, 592–595.

15. C. Feldmann, M. Roming, and K. Trampert, *Small*, 2006, **2**, 1248–50.

16. Z. Quan, D. Yang, P. Yang, X. Zhang, H. Lian, X. Liu, and J. Lin, *Inorg. Chem.*, 2008, **47**, 9509–17.

17. P. Aubry, A. Bensalah, P. Gredin, G. Patriarche, D. Vivien, and M. Mortier, *Opt. Mater. (Amst).*, 2009, **31**, 750–753.

18. K. Landfester, *Annu. Rev. Mater. Res.*, 2006, **36**, 231–279.

19. P. Dolcet, M. Casarin, C. Maccato, L. Bovo, G. Ischia, S. Gialanella, F. Mancin, E. Tondello, and S. Gross, *J. Mater. Chem.*, 2012, **22**, 1620–1626.

20. P. Dolcet, F. Latini, M. Casarin, A. Speghini, E. Tondello, C. Foss, S. Diodati, L. Verin, A. Motta, and S. Gross, *Eur. J. Inorg. Chem.*, 2013, **2013**, 2291–2300.

21. E. Butturini, P. Dolcet, M. Casarin, A. Speghini, M. Pedroni, F. Benetti, A. Motta, D. Badocco, P. Pastore, S. Diodati, L. Pandolfo, and S. Gross, *J. Mater. Chem. B*, 2014, **2**, 6639–6651.

22. P. Dolcet, C. Maurizio, M. Casarin, L. Pandolfo, S. Gialanella, D. Badocco, P. Pastore, and S. Gross, *Eur.J.Inorg.Chem.*

23. M. Pedroni, F. Piccinelli, T. Passuello, S. Polizzi, J. Ueda, P. Haro-González, L. Martinez Maestro, D. Jaque, J. García-Solé, M. Bettinelli, and A. Speghini, *Cryst. Growth Des.*, 2013, **13**, 4906–4913.

24. I. Lonardelli, H. R. Wenk, L. Lutterotti, and M. Goodwin, *J. Synchrotron Radiat.*, 2005, **12**, 354–360.

25. L. Lutterotti, S. Matthies, H.-R. Wenk, A. S. Schultz, and J. Richardson J.W., *J. Appl. Phys.*, 1997, **81**, 594–600.

26. D. H. Templeton and C. H. Dauben, *J. Am. Chem. Soc.*, 1954, **76**, 5237–5239.

27. R. Shannon, *Acta Crystallogr. A*, 1976, **32**, 751–767.

28. A. V Naumkin, A. Kraut-Vass, S. W. Gaarenstroom, and C. J. Powell, .

29. J. M. F. Moulder, W. F. Stickle, P. E. Sobol, and K. D. Bomben, *Handbook of X-Ray Photoelectron Spectroscopy*, Perkin-Elmer Corporation, Eden Praire, 2nd edn., 1992.

30. P. Samuel, H. Ishizawa, Y. Ezura, K. I. Ueda, and S. M. Babu, *Opt. Mater. (Amst).*, 2011, **33**, 735–737.

31. P. W. Loeffen, R. F. Pettifer, S. Müllender, M. van Veenendaal, J. Röhler, D. S. Sivia, M. A. Van Veenendaal, S. Mu, and J. Ro, *Phys. Rev. B*, 1996, **54**, 14877–14880.

32. E. Wiberg, A. F. Holleman, and N. Wiberg, *Lehrbuch Der Anorganischen Chemie*, Walter de Gruyter, Berlin, 101st edn., 1995.

33. L. Song and L. Xue, *Appl. Surf. Sci.*, 2012, **258**, 3497–3501.

34. L. Song, J. Gao, and J. Li, *J. Lumin.*, 2014, **151**, 18–21.

35. B. Ritter, T. Krahl, K. Rurack, and E. Kemnitz, *J. Mater. Chem. C*, 2014, **2**, 8607–8613.

36. C. M. Dodson and R. Zia, *Phys. Rev. B - Condens. Matter Mater. Phys.*, 2012, **86**.

37. M. D. Faucher and P. A. Tanner, *J. Phys. Condens. Matter*, 2006, **18**, 8503–8522.

38. S. Fujihara, *J. Appl. Phys.*, 2004, **95**, 8002.

39. V. Petit, P. Camy, J. L. Doualan, X. Portier, and R. Moncorgé, *Phys. Rev. B - Condens. Matter Mater. Phys.*, 2008, **78**.

40. P. Hänninen and H. Härmä, *Lanthanide Luminescence: Photophysical, Analytical and Biological Aspects*, Springer, Heidelberg, 2011.

41. G. Lakshminarayana, R. Yang, M. Mao, J. Qiu, and I. V. Kityk, *J. Non. Cryst. Solids*, 2009, **355**, 2668–2673.

42. D. Briggs and M. P. Seah, *Practical Surface Analysis: Auger and X-ray photoelectron spectroscopy*, Wiley, New York, 1990, vol. 2nd.

43. D. Shirley, *Phys. Rev. B*, 1972, **5**, 4709–4714.

44. W. T. Carnall, P. R. Fields, and K. Rajnak, *J. Chem. Phys.*, 1968, **49**, 4424.

45. S. Thomas, R. George, S. Nayab Rasool, M. Rathaiah, V. Venkatramu, C. Joseph, and N. V. Unnikrishnan, *Opt. Mater. (Amst).*, 2013, **36**, 242–250.

46. B. Ravel and M. Newville, *J. Synchrotron Radiat.*, 2005, **12**, 537–41.

